Journal of Materials Chemistry A

Nanoengineered Au-Carbon Nitride Interfaces Enhance Photo-Catalytic Pure Water Splitting

Journal:	*Journal of Materials Chemistry A*
Manuscript ID	TA-ART-08-2023-005201
Article Type:	Paper
Date Submitted by the Author:	30-Aug-2023
Complete List of Authors:	Silva, Ingrid; Universidade Federal de Minas Gerais, Chemistry; Max Planck Institute of Colloids and Interfaces, Department of Colloid Chemistry Roy, Soumyabrata; Rice University, Department of Materials Science and NanoEngineering Kumar, Pawan; University of Calgary, Chemical and Petroleum Engineering Chen, Zhi Wen; University of Toronto, ; Jilin University, Teixeira, Ivo; Max Planck Institute of Colloids and Interfaces, Campos-Mata, Astrid; Rice University, Department of Materials Science and NanoEngineering Mosqueira Antônio, Loudiana; Federal University of Minas Gerais, Department of Phisics Ladeira, Luiz; Federal University of Minas Gerais, Department of Physics Stumpf, Humberto; Universidade Federal de Minas Gerais, Departamento de Química; Singh, Chandra Veer; University of Toronto, Material Science and Engineering de Carvalho Teixeira, Ana Paula; Universidade Federal de Minas Gerais, Chemistry Kibria, Md; University of Calgary, Chemical and Petroleum Engineering Ajayan, Pulickel; Rice University, Mechanical Engineering and Materials Science

ARTICLE

Nanoengineered Au-Carbon Nitride Interfaces Enhance Photo-Catalytic Pure Water Splitting

Received 00th January 20xx,
Accepted 00th January 20xx

DOI: 10.1039/x0xx00000x

Ingrid F. Silva,[#,a,b] Soumyabrata Roy,[#,*,c] Pawan Kumar,[#,d] Zhiwen Chen,[e] Ivo F. Teixeira,[f] Astrid Campos-Mata,[c] Loudiana M. Antônio,[g] Luiz O. Ladeira,[g] Humberto O. Stumpf,[a] Chandra Veer Singh,[e] Ana Paula C. Teixeira,[a] Md Golam Kibria,[*,d] Pulickel M. Ajayan.[*,c]

Photocatalytic pure water splitting using solar energy is one of the promising routes to produce sustainable green hydrogen (H_2). Tuning the interfacial active site density at catalytic heterojunctions and better light management are imperative to steer the structure-activity correlations to enhance the photo-efficiency of nanocomposite photocatalysts. Herein, we report the decoration of nitrogen defects-rich carbon nitride CN(T) with metallic Au nanostructures of different morphologies and sizes to investigate their influence on the photocatalytic hydrogen evolution reactions (HER). The CN(T)-7-NP nano-heterostructure comprises Au nanoparticles (NPs) of ~7 nm and thiourea-derived defective CN exhibits an excellent H_2 production rate of 76.8 µmol g^{-1} h^{-1} from pure water under simulated AM 1.5 solar irradiation. In contrast to large-size Au nanorods, the high activity of CN(T)-7-NP was attributed to their strong localized surface plasmon resonance (LSPR) mediated visible absorption and interfacial charge separation. The surface ligands used to control Au nanostructures morphology were found to play a major role in the stabilization of NPs and improve interfacial charge transport between Au NPs and CN(T). First-principles calculations revealed that defects in CN and Au-CN interfacial sites in these nanocomposites facilitate the separation of e^-/h^+ pairs after light excitation and provide lower energy barrier pathways for H_2 production by photocatalytic water splitting.

Introduction

Hydrogen (H_2), with the highest gravimetric energy density (142 MJ kg^{-1}), ubiquitous industrial usage (e.g. NH_3 synthesis) and benign combustive byproduct (water), is the ideal energy carrier for sustainable energy infrastructure.[1,2] However, more than 95% of the world's hydrogen is currently produced through energy-intensive steam methane reforming (SMR), with a heavy carbon footprint ("gray hydrogen").[3,4] While coupling SMR with carbon capture and storage technologies to produce the so-called "blue hydrogen" have garnered some industrial traction, the true carbon footprint projections of this technology still remain elusive.[5] Thus, electrolytic water splitting powered by renewable electricity (RE) remains the most viable route to produce truly "green hydrogen". However, expensive grid storage, intermittency and significant energy loss during the direct current (DC) to alternating current (AC) transformation for long-distance transfer, present critical challenges for using RE for green H_2 production.[6] Photocatalytic hydrogen generation by using direct sunlight and pure water is the most promising and greenest approach to trap inexpensive solar energy in chemical bonds for ubiquitous and on-demand usage.[1,4] This has led to extensive research on designing band gap tuned semiconductor catalysts for the effective use of solar energy and abundantly available water to generate H_2.[7–9]

Graphitic carbon nitride (g-C_3N_4, CN), a conjugated polymeric semiconductor, has emerged as the "holy grail" of next-generation photocatalysts for hydrogen evolution reaction (HER), replacing the traditional wide band gap semiconductor metal oxides such as TiO_2, ZnO, WO_3, $BiVO_4$, *etc.*[8,10] CN possess a moderate bandgap (~ 2.7 eV) for enhanced solar energy absorption and appropriate conduction (-1.1 eV) and valence (1.6 eV) band potentials to catalyze the overall water splitting reaction. In addition, facile and low-cost synthesis, chemical stability, easy functionalization routes, and electronic structure tunability make CN a promising photocatalytic platform for H_2 evolution from water.[8,10] Nevertheless, CN's photocatalytic efficiency for HER remains too low for practical applications due to the lack of visible-light absorption beyond 460 nm, poor electrical conductivity and prodigious recombination rate of photogenerated charge carriers (e^-/h^+ pairs).[10,11] Several strategies have been extensively explored to improve the CN's

[a.] *Departamento de Química, ICEx, Universidade Federal de Minas Gerais, Belo Horizonte, MG, 31270-901, Brazil.*
[b.] *Department of Colloid Chemistry, Max Planck Institute of Colloids and Interfaces, Am Mühlenberg 1, D-14476 Potsdam, Germany.*
[c.] *Department of Materials Science and NanoEngineering, Rice University, Houston, Texas 77005, USA.*
[d.] *Department of Chemical and Petroleum Engineering, University of Calgary, 2500 University Drive, NW Calgary, Alberta, T2N 1N4, Canada.*
[e.] *Department of Material Science and Engineering, University of Toronto, Ontario, Canada.*
[f.] *Departamento de Química, Universidade Federal de São Carlos, São Carlos, SP, 13565-905, Brazil.*
[g.] *Departamento de Física, ICEx, Universidade Federal de Minas Gerais, Belo Horizonte, MG, 31270-901, Brazil.*
[#]Equal contribution.
Electronic Supplementary Information (ESI) available: [details of any supplementary information available should be included here]. See DOI: 10.1039/x0xx00000x

photocatalytic performance in HER, such as doping with heteroatoms (P, F, S, *etc.*), surface modification, heterojunction formation, metal complexes sensitization, *etc*.[10,12] The chemical structure modification of CN by alteration of heptazine (C_6N_7) units, and incorporation of N- or C-rich units to manipulate C/N stoichiometry are widely adopted approaches to improve the visible absorption and reduce charge recombination kinetics.[13–15] The chemical nature of precursor molecules governs the C/N stoichiometric ratio and degree of polymerization, which concomitantly reinforce optical bandgap properties and facilitate better charge migration.[14] Previous reports demonstrate that thermal condensation of smaller precursor molecules such as urea proceeds *via* massive gas evolution compared to large N-rich precursors (i.e., dicyandiamide, melamine) leading to a high C/N ratio due to the peeling effect of oxygen-functionalities.[16,17] The N-deficient sites in resulting CNs, provide active centers for better accommodation of photogeneration charge to boost the photocatalytic performance. The photocatalytic performance of CN-based catalysts can be further improved by the decoration of noble metals nanostructures that work as electron sinks and also increase visible absorption *via* Localized Surface Plasmon Resonance (LSPR) enhancement.[9,15,18]

Excitation by LSPR in plasmonic nanoparticles (NPs) can improve the absorption profile of semiconductors *via* low energy inter-band (d→sp) transition and effective trapping of photoexcited electrons due to low-lying Fermi level compared to semiconductors.[19] The LSPR effect enhances the photocatalytic HER by the generation of hot electrons, resonant energy transfer, local electromagnetic field enhancement and direct electron transfer.[20] The LSPR frequency depends on the size, shape, composition and structure of the NPs, as well as the environment dielectric constant.[19] Gold (Au) NPs are enticing candidates for plasmon-mediated carrier transfer research due to their strong plasmonic resonance under visible light or near-infrared ranges, and their ability to form Schottky barriers with semiconductors like CNs and TiO_2.[19,20] Various protocols such as photoreduction, impregnation and deposition-precipitation are employed to decorate Au NPs on semiconductor surfaces.[10] Furthermore, ligands play important roles in the rational design of these NPs, such as size, shape, and interparticle spacing, and also in determining the properties of the interface between the NPs and semiconductors.[21,22] There are different types of surface capping agents, such as cetyltrimethylammonium bromide (CTAB), which are often used for seed growth. Other specific functional groups such as thiols (–SH) are usually required to link Au NPs to the semiconductor through gold–sulfur (Au–S) bonding, once it improves the interfacial contact and also tunes the work function.[23] These molecules act as small gaps that prevent direct contact of Au NPs with the desired surface and can contribute to the plasmon damping mechanism impairing the photocatalytic performances.[23,24] Many reports demonstrate Au NPs in different morphological states can synergistically enhance the performance of CNs. For instance, Guo and co-workers displayed that Au NPs can play a dual role, acting as both a metal plasmon and a cocatalyst, to enhance the performance of Au/CN reaching a hydrogen evolution rate of 159.9 μmol g^{-1} h^{-1} in the presence of triethanolamine (TEOA) as a sacrificial donor.[20] In another study, Tian *et al.* demonstrated Au nanorods (NRs) and CN heterostructure can ameliorate the H_2 evolution rate 4 times (350.6 μmol g^{-1} h^{-1}) compared to Pt/CNs (68.9 μmol g^{-1} h^{-1}) under visible light irradiation and TEOA.[25] Despite all these efforts, the exact contribution of the shape and size of Au NPs on photocatalytic performance remains obscured. Furthermore the use of sacrificial donors during the photocatalytic experiments is highly undesirable for green H_2 production.

Herein, we control the shape, size, and ligands of Au nanostructures (NPs and NRs) embedded in defective CN, to evaluate their influence on photocatalytic HER under solar irradiation. The integration of Au in CN scaffolds was found to deliver enhanced photo-splitting of pure water due to size and shape-dependent LSPR, better charge separation and co-catalysis effects. The heterostructure with the smallest spherical Au NPs, (CN(T)-7-NP), displayed the highest H_2 production rate of 76.8 μmol g^{-1} h^{-1} from pure water under AM1.5G irradiation. Furthermore, the Au metal shape and size dictates LSPR and interfacial charge separation in the Au/N-deficient heptazine framework. Removal of surface ligands used to control Au nanoarchitectures by thermal annealing followed by photocatalytic experiments demonstrates reduced H_2 evolution, due to hindered charge transfer from Au NPs to CN surface and vice versa. First principles calculations revealed that defects in the CN matrix and Au-CN interfacial sites in the composite could facilitate the separation of charge carriers and provide lower energy barrier pathways for H_2 production by photo-splitting of water.

Results and Discussion

Syntheses, structural analyses and properties of Au-CN nanocomposites

The synthetic strategy for the Au-CN nano-heterostructures is schematically shown in **Figure 1**. Two types of CNs, CN(M) and CN(T), were synthesized by thermal polycondensation of melamine and thiourea, respectively, at 550 °C for 30 min, using a ramp rate of 10 °C min^{-1}.[26] Subsequently, the Au-CN(T) composites were synthesized using the incipient wetness (IW) method (see SI for more details). Firstly, the Au metal solutions were prepared with different average diameters and shapes (Au-7-NP, Au-14-NP, Au-65-NR and Au-15-NR), by varying the synthetic conditions and surfactants as per previously reported methods.[27–29] Au NPs solutions were prepared with different reducing agents, sodium borohydride ($NaBH_4$) and trisodium citrate (TSC), for Au-7-NP and Au-14-NP, respectively, which allowed control of NPs sizes. In addition, for Au-7-NP, glutathione (GSH) was used during synthesis, leading to a more effective bonding between this capping agent and the NPs (Au-S). On the other hand, to control the NRs sizes, different amounts of seed solutions were used in their synthesis containing the CTAB surfactant. Next, the Au dispersions in water were added dropwise into CN(T) powder material at a controlled temperature of 90 °C, mixed and dried to achieve a

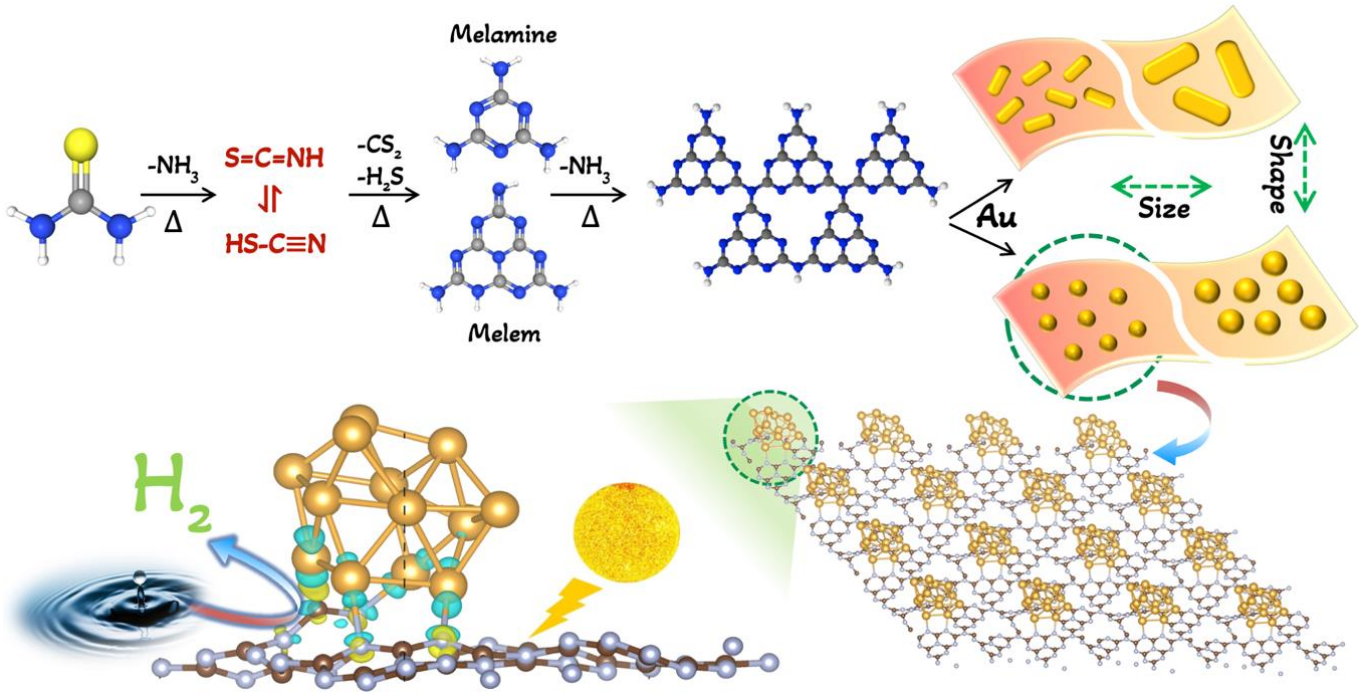

Figure 1. Synthetic protocol for the CN(T) using thiourea precursor followed by decoration of Au nanostructures. The enlarged part at bottom left displayed effective interfacial contact between CN(T) and Au NPs due to charge delocalization.

uniform and homogeneous impregnation of the nanostructures. Several cycles of IW impregnation were conducted until the full utilization of Au metal solutions. The Au nanostructures contents in these solutions were calculated by inductively coupled plasma-optical emission spectrometry (ICP-OES) analysis making it possible to pre-calculate the solutions amounts added in this last step. The obtained solid powders of the Au-CN nanocomposites were dried under vacuum for 24 h and coded as CN(T)-7-NP, CN(T)-14-NP, CN(T)-65-NR, CN(T)-15-NR for respective morphologies and sizes.

The synthesized nanocomposites comprising CN(T) and gold nanostructures (Au-CN(T)) were characterized by elemental analysis and the obtained results are shown in **Table 1**. The "perfect" graphitic CN consists of interconnected π-conjugated planar 2D sheets of poly(tri-s-triazines) linked by tertiary amines lacking basic activity related to the NH bridge's presence.[10] The presence of hydrogen is attributed to incomplete condensation of the monomeric units leaving residual -NH_2 functionalities at the edges and H-bonded region within the sheets. The high H contents of CN(T) and Au-CN(T) nanocomposites demonstrate that thiourea promotes incomplete condensation of heptazine (C_6N_7) units leaving stranded -NH_2 moieties, which serves as defect sites in the structure of these materials compared to CN(M).[26] In addition, sulfur traces were noticed in the materials produced from thiourea, demonstrating that there are some defects related to the presence of sulfur in the C_6N_7 units.[30,31] The highest S content was found for CN(T)-7-NP, due to the usage of the S-rich glutathione precursor for the synthesis of Au NPs. Interestingly, all materials have between 0.1-0.2% gold in their structures. Furthermore, the H and C contents in CN(T)-65-NR and CN(T)-15-NR are higher than the other materials due to the presence of CTAB in these Au-NR nanostructures syntheses. The N/C ratio of CN(M) and CN(T) was calculated to be 1.57 and 1.55 which was close to the theoretical N/C ratio for CNs (1.55).[32]

The fine structural attributes of the pristine CNs and Au decorated nanocomposites (Au-CN) were determined using high-resolution transmission electron microscopy (HRTEM). The

Table 1. C, H, N, S and Au contents for synthesized materials

Materials	C (%)	H (%)	N (%)	S (%)	Au (%)
CN(M)	34.62 (±0.05)	1.97 (±0.05)	54.46 (±0.32)	0.04 (±0.01)	-
CN(T)	33.34 (±0.03)	2.17 (±0.01)	51.88 (±0.06)	0.64 (±0.01)	-
CN(T)-7-NP	30.65 (±0.05)	2.53 (±0.01)	43.76 (±0.20)	1.31 (±0.04)	0.15 (±0.04)
CN(T)-14-NP	33.14 (±0.06)	2.16 (±0.01)	51.30 (±0.46)	0.12 (±0.01)	0.13 (±0.01)
CN(T)-65-NR	34.30 (±0.05)	2.38 (±0.01)	51.20 (±0.03)	0.11 (±0.01)	0.19 (±0.05)
CN(T)-15-NR	37.79 (±0.31)	3.58 (±0.09)	46.19 (±0.51)	0.09 (±0.01)	0.23 (±0.06)

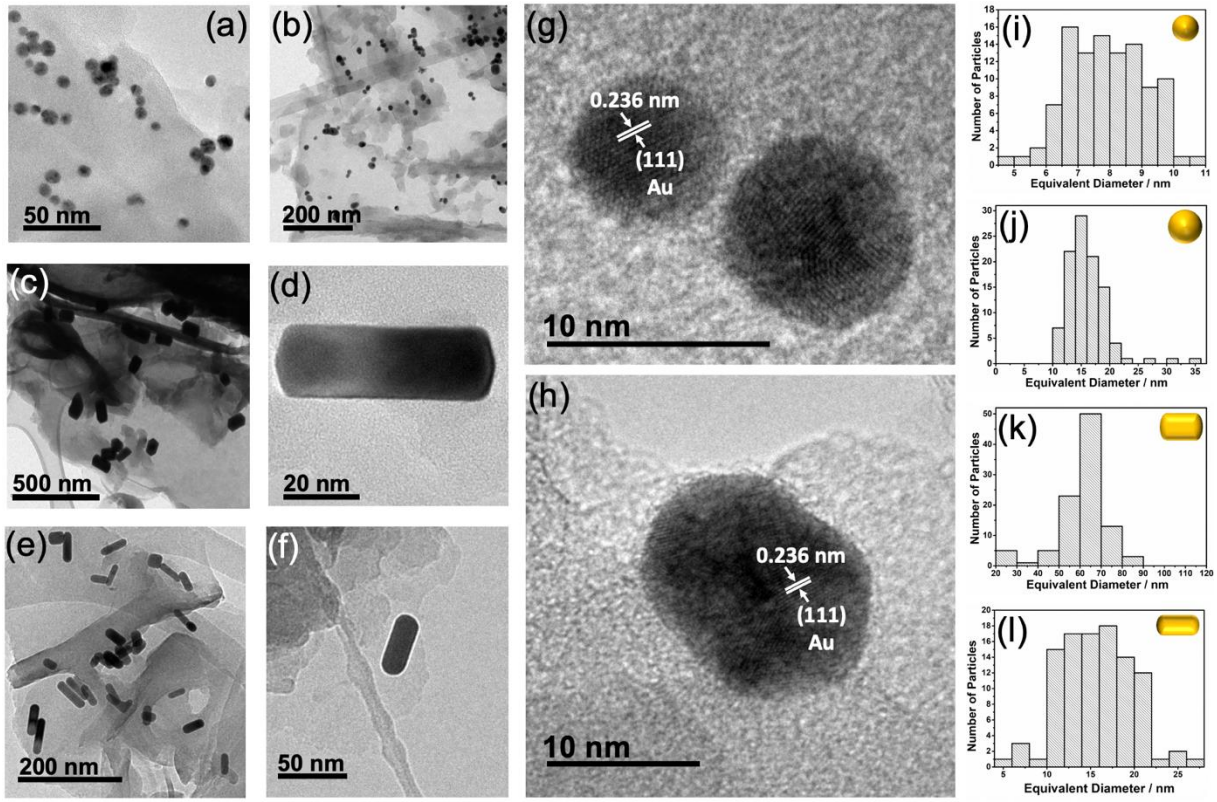

Figure 2. TEM images and particles diameter distribution for the Au-CNs nanocomposites. **a**, **g** and **i)** CN(T)-7-NP; **b**, **h** and **j)** CN(T)-14-NP; **c**, **d** and **k)** CN(T)-65-NR; **e**, **f** and **l)** CN(T)-15-NR.

HRTEM images obtained for CN(T) and CN(M) materials show the variation in morphology of these previously reported materials (**Figure S1**).[26] The carbon nitride matrix was found to be composed of thin stacked 2D sheets agglomerated together due to intersheet hydrogen bonding. The HRTEM images of CN(M) at high magnification displayed localized lattice fringes with 0.33 nm spacing suggesting populated stacking in the bulk material (**Figure S1a-b**). The lattice fringe patterns almost disappeared for CN(T), indicating this material presented less crystallinity than CN(M) due to the presence of defects (**Figure S1c-d**). Au nanostructures on the CN were well distributed on the 2D sheets across all samples with some clustering points (**Figures 2a-f and S2**). Au NPs sizes were modulated by the reducing agent added in their syntheses, using sodium borohydride, a strong reducing agent, and a solution of TSC (1% w/v) for the Au-7-NP and Au-14-NP syntheses, respectively. The sizes of Au NRs were controlled by the seed solution amount added in the growth solutions, in which Au-65-NR and Au-15-NR were prepared with 12 µL and 500 µL of the seed solution, respectively. The HRTEM images of CN(T)-7-NP and CN(T)-14-NP show spherical and oval, dense crystalline Au NPs embedded in CN(T) respectively. Distinct lattice fringes with an interplanar d-spacing of 0.236 nm were attributed to the (111) planes of face-centered cubic (FCC) Au (**Figures 2g-h**).[33] **Figures 2i and 2j** display the corresponding particle diameter distribution histograms for CN(T)-7-NP and CN(T)-14-NP. The NPs used for the preparation of these materials have diameters ranging, mainly, between 6-10 nm and 10-20 nm for CN(T)-7-NP and CN(T)-14-NP, respectively. The HRTEM images of CN(T)-65-NR show the presence of NRs with cylindrical and cubic shapes having particle diameter distribution mainly between 60-70 nm (**Figures 2c-d, k**). On the other hand, CN(T)-15-NR material exhibited a cylindrical NR structure without a trace of any other morphologies and the particle size distribution shows diameters around 10-22 nm (**Figures 2e-f, l**).

The powder XRD diffractograms of CN(M) and CN(T) showed peaks at 13.0° and 27.4°, which are characteristic of CN-based materials and indexed to (100) and (002) planes of CNs (**Figure 3a**).[26] Interestingly, the (002) peak intensity of CN(T) was decreased compared to CN(M) indicating the less populated intersheet stacking in the porous structure.[34] The XRD patterns of Au-CN(T) nanocomposites also exhibited similar diffraction patterns as that of pure CNs along with four additional diffraction peaks corresponding to metallic Au. The gold peaks in the nanocomposites appear at 38.1°, 44.3°, 64.5° and 77.6° which can be assigned to (111), (200), (220) and (311) planes, respectively, of metallic gold (Au^0) with cubic structure (JCPDS Card No. 04-0784) (**Figure 3a**).[35,36] This confirms the successful distribution and impregnation of Au nanostructures on the defective CN matrix. Noticeably, the peaks corresponding to Au are broad and weak with the lack of intense peaks at higher angles confirming the absence of significantly larger particles in the composites.[35] Further, synchrotron-based wide-angle X-ray scattering (WAXS) of CN(T) also displayed (002) peak broadening compared to CN(M) validating the reduced intersheet stacking.[37] Additionally, all the peaks of metallic gold were clearly observable in wide-angle X-ray scattering (WAXS) profile of CN(T)-7-NP composite (**Figure S3**).

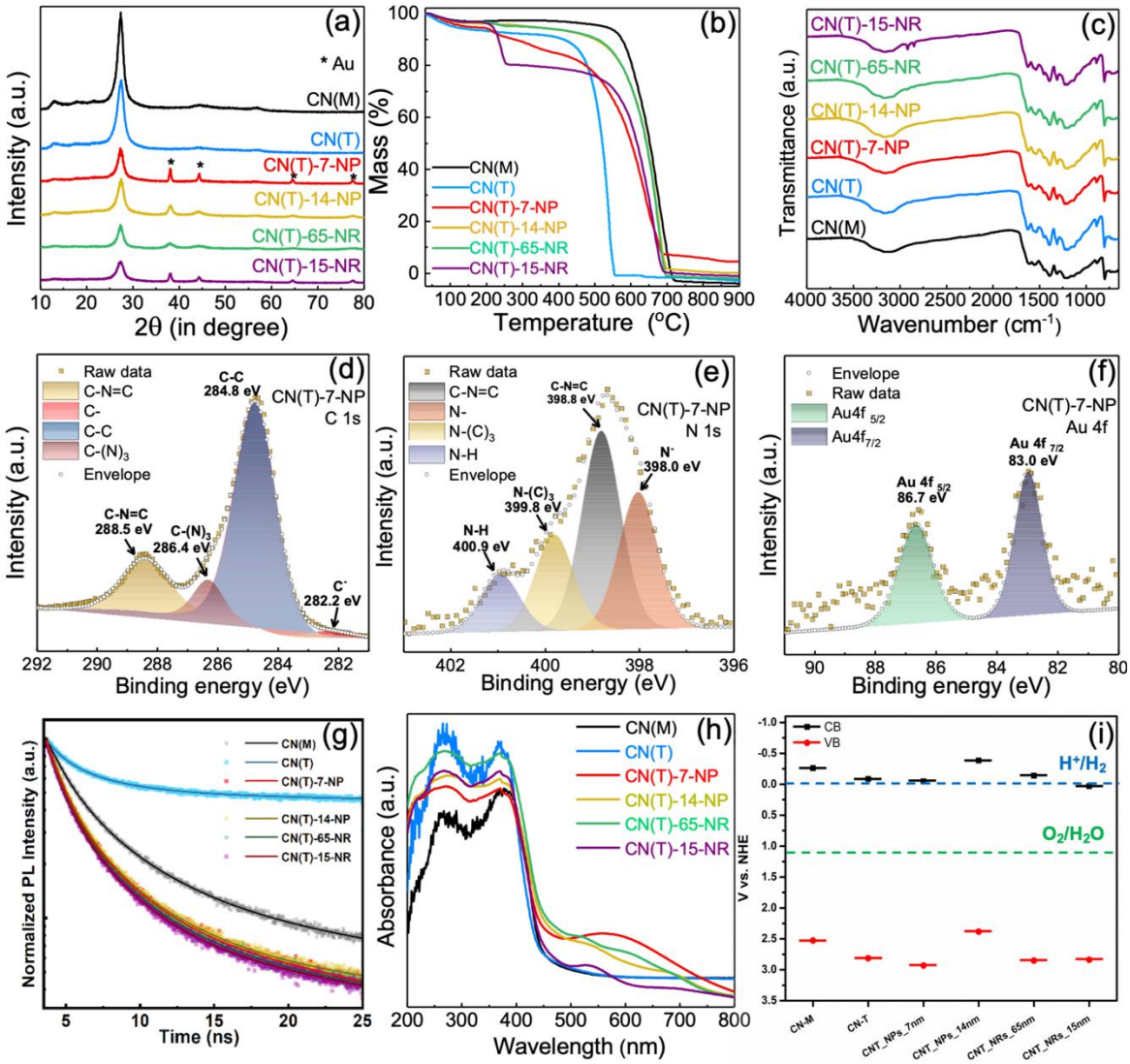

Figure 3. (a) XRD patterns; **(b)** TG curves performed in dynamic synthetic air atmosphere (50 mL min^{-1}) in alumina crucible with 10 °C min^{-1} heating rate; **(c)** FT-IR spectra; **(d)** Time resolved photoluminescence (TRPL) spectra (excitation wavelength 370 nm); **(e)** Diffuse reflectance UV-Vis spectra; **(f)** Values of the conduction bands (CB) and valence bands (VB) of the synthesized materials estimated from the Motty-Schottky experiments; Core-level high-resolution XPS spectra of CN(T)-7-NP in **(g)** C 1s, **(h)** N 1s and **(i)** Au 4f regions.

The bulk average sizes of the Au nanostructures were also calculated by fitting the Au peaks in the XRD diffractograms with Gaussian profiles (**Figure S4**). The average Au nanostructure diameters were found to be 5.04 nm, 15.62 nm, 15.79 nm and 11.42 nm for CN(T)-7-NP, CN(T)-14-NP, CN(T)-65-NR and CN(T)-15-NR materials, respectively, using the Scherrer equation (**Eq. S1**). Holder and Schaak pointed out the limitations of the Scherrer equation for calculating crystalline domain sizes in particles ranging from 1 µm to 50 nm, alongwith size anisotropy. In such cases, peak broadening can be predominantly influenced by instrumental effects, strain etc. rather than the particle size effect, alone.[38] This could explain the discrepancy in Au particle size of the CN(T)-65-NR material between the XRD and TEM techniques, 15.79 nm and 60-70 nm, respectively. The calculated sizes for the other materials were found to be close to those obtained from TEM images, indicating some consistency between the two methods.

The thermogravimetric (TG) and differential thermogravimetry (DTG) curves obtained under air atmosphere showed good thermal stability of the CNs and Au-CN(T) nanocomposites up to ~410 °C, which is characteristic of carbon nitride-based materials (**Figures 3b and S5**). A small weight loss of ~4% around 100 °C for all materials was assigned to the loss of surface adsorbed moisture present in the materials.[26] Compared to CN(M), the CN(T) presented lower thermal stability, which can be associated with the higher amount of defects and less stacked structure prone to thermal degradation, in agreement with HRTEM images. The gold materials CN(T)-7-NP, CN(T)-65-NR and CN(T)-15-NR showed an intermediate loss of 4, 2 and 16%, respectively, between 170-280 °C, related to the degradation of stabilizing ligands used in the Au nanostructures synthesis. Furthermore, a sharp weight loss, in the temperature range of 450 to 620 °C was attributed to the decomposition of the C_6N_7 units of carbon nitrides.[26] Interestingly, CN(T)-7-NP showed a gradual loss of about 20% until the beginning of the C_6N_7 units decomposition, which is correlated to the strong Au-S binding between the glutathione ligand and Au NPs. On the other hand, the CN(T)-15-NR showed the same amount of

weight loss until the CN decomposition, but faster, which is associated with the weak binding between the CTAB ligand and Au NRs. The residue observed in the TGA curves of the gold nanocomposites can be attributed to the gold remaining in the samples and inorganic carbon residue. FTIR spectra for all the composites showed characteristic stretching frequencies of carbon nitride-based materials similar to earlier reports without any significant difference in the bands (**Figure 3c**).[4,26] The samples displayed the typical bands for heptazine-based carbon nitrides, i.e. at 1630 and 1560 cm^{-1} ($\nu_{C=N}$), 1450, 1315, 1230 and 1200 cm^{-1} (ν_{C-N} of C_6N_7 heterocycle) and strong band at 804 cm^{-1} (breathing mode of the triazine ring (C_3N_3) of CN heterocyclic units).[26] In addition, the region between 3500 and 3000 cm^{-1} shows the broad stretching modes originating from the combined stretching of surface adsorbed -OH and residual N–H functionalities, which implies the existence of uncondensed amino groups (=NH and/or -NH_2) in the two dimensional (2D) CN sheets, as observed in the elemental analysis.[26] Interestingly, the CN(T) containing samples displayed a shoulder peak at the higher frequency (3320 cm^{-1}) merged in large band suggesting higher population of N-H functionalities in CN(T) compared to CN(M).[39] Furthermore, CN(T)-65-NR and CN(T)-15-NR materials showed bands at 2920 and 2851 cm^{-1} related to the ν_{C-H} of CTAB ligand used in Au NRs syntheses. It was not possible to resolve the bands for the other ligands used in the NPs synthesis, due to their overlapping frequencies with the CNs bands.

The surface composition and electronic states of the elements for the Au-CN nanocomposites were analyzed by X-ray photoelectron spectroscopy (XPS) survey scans and core-level high-resolution spectra for C 1s, N 1s and Au 4f using the peak deconvolution method (**Figures 3d-fand S6**). The C 1s spectrum of CN(T)-7-NP can be deconvoluted into four peaks at 282.2, 284.8, 286.4 and 288.5 eV, which can be attributed to negatively charged carbon atoms C^-, uncondensed/adventitious (C-C), tertiary sp^2 carbon atoms bonded to three nitrogen in C_6N_7 ring ($C-(N)_3$) and secondary sp^2- N-C=N carbons, respectively (**Figure 3d**).[36,40] For the CN(T)-14-NP and CN(T)-15-NR heterostructures the first peak at lower BE corresponded to negatively charged carbon atoms and was not observed suggesting plenty of defect-rich state in CN(T)-7-NP (**Figure S6a-c**). The N 1s spectrum of CN(T)-7-NP can be fitted into four peaks located at 398.0, 398.8, 399.6 and 400.5 eV attributed to deprotonated nitrogen atoms N^-, the sp^2-hybridized secondary (C-N=C), tertiary ($N-(C)_3$) and sp^3 primary nitrogen atom ($N-H/NH_2$), respectively (**Figure 3e**).[36,40] CN(T)-14-NP, CN(T)-65-NR and CN(T)-15-NR nanocomposites showed similar N 1s spectra as obtained for CN(T)-7-NP (**Figure S6d-f**). In addition, Au 4f XPS spectrum of CN(T)-7-NP exhibited two well-separated peaks positioned at 83.0 and 86.7 eV corresponding to Au $4f_{7/2}$ and Au $4f_{5/2}$ components of Au present in metallic state (**Figure 3f**).[36] Other Au-CN(T) nanocomposites also demonstrated similar Au 4f surface composition for CN(T)-14-NP, CN(T)-65-NR and CN(T)-15-NR materials (**Figure S6g-i**). The obtained results further confirm the existence of metallic Au integrated into the CN matrices across all the composites. The C K-edge and N K-edge near edge X-ray absorption fine structure (NEXAFS) of CNs and Au-embedded CN structure displayed characteristics (π* and σ*) transitions suggesting well-constituted CN matrix which remain intact in all heterostructures (**Figure S7**).

Photoluminescence (PL) emission corresponds to the recombination of photogenerated electrons and holes and is useful to understand the efficiency of electron transfer and e^-/h^+ pairs separation in the nanocomposites.[41] Time-resolved photoluminescence (TRPL) spectra of materials were collected to understand the mechanism of the charge carrier's recombination process using a 370 nm excitation single photon pulsed laser (**Figure 3g**). The acquired PL lifetime decay curve was fitted tri-exponentially as reported previously for carbon nitride-based materials using the following equation:

$$I(t)=A_1e^{-t/\tau1} + A_2e^{-t/\tau2} + A_3e^{-t/\tau3} \quad \textbf{Eq. 1}$$

where, A_1, A_2 and A_3 represent the normalized amplitudes of each decay component and τ_1, τ_2 and τ_3 are values of the lifetime components, respectively.[42,43] The derived lifetime value and their fractional contributions are listed in **Table S1**.

The tertiary N-linked heptazine (C_6N_7) units in carbon nitride constituted alternate C-N sp^2 and C-N sp^3 hybridized systems. The sp^3 C-N coordination produces high energy σ and σ* molecular orbital (MO) while π and π* MO resulted from sp^2 C-N bonding. Apart from this, the lone pairs (LP) on secondary nitrogen ($:N-C_2$) can participate in conjugation, therefore, creating low gap (LP+π) bonding (valence band) and antibonding (conduction band) hybrid orbital therefore carbon nitride absorbs in the visible region.[44,45]

The first two shorter lifetime components originated from the direct band-to-band recombination of (σ*→σ and π*→(LP+π)) excited electrons. Another component with a relatively larger lifetime originated from the σ*→π* non-radiative intersystem crossing (ISC) followed by π*→(LP+π) radiative recombination.[46–48] Furthermore, low energy trap sites (defects) mediated recombination also contributes to the third-lifetime component.[49] In regular carbon nitride (CN(M)), the value of the third lifetime was found to be 6.9 ns which increased to 7.96 ns in defect-rich CN(T). From these observations, it is clear that N-deficient CN(T) prolonged the charge recombination time due to the stabilization of generated charge in N-vacancies. Interestingly, after the integration of gold nanoparticles, the value of the third lifetime was reduced suggesting that Au nanostructures can reduce trap-assisted recombination due to the accommodation of some charge. Furthermore, the average lifetime (τ_{avg}) which depicts the cumulative recombination process was calculated from the three-lifetime components using the following equation.

$$\tau_{avg}= (A_1\tau_1^2+A_2\tau_2^2+A_3\tau_3^2)/(A_1\tau_1+A_2\tau_2+A_3\tau_3) \quad \textbf{Eq.2}$$

It is clear from **Table S1** that the τ_{avg} value for CN(T) was increased (6.75 ns) compared to CN(M) (5.18 ns) due to the stabilization of photogenerated charge in populated defects which is beneficial for the photocatalytic process. The value of

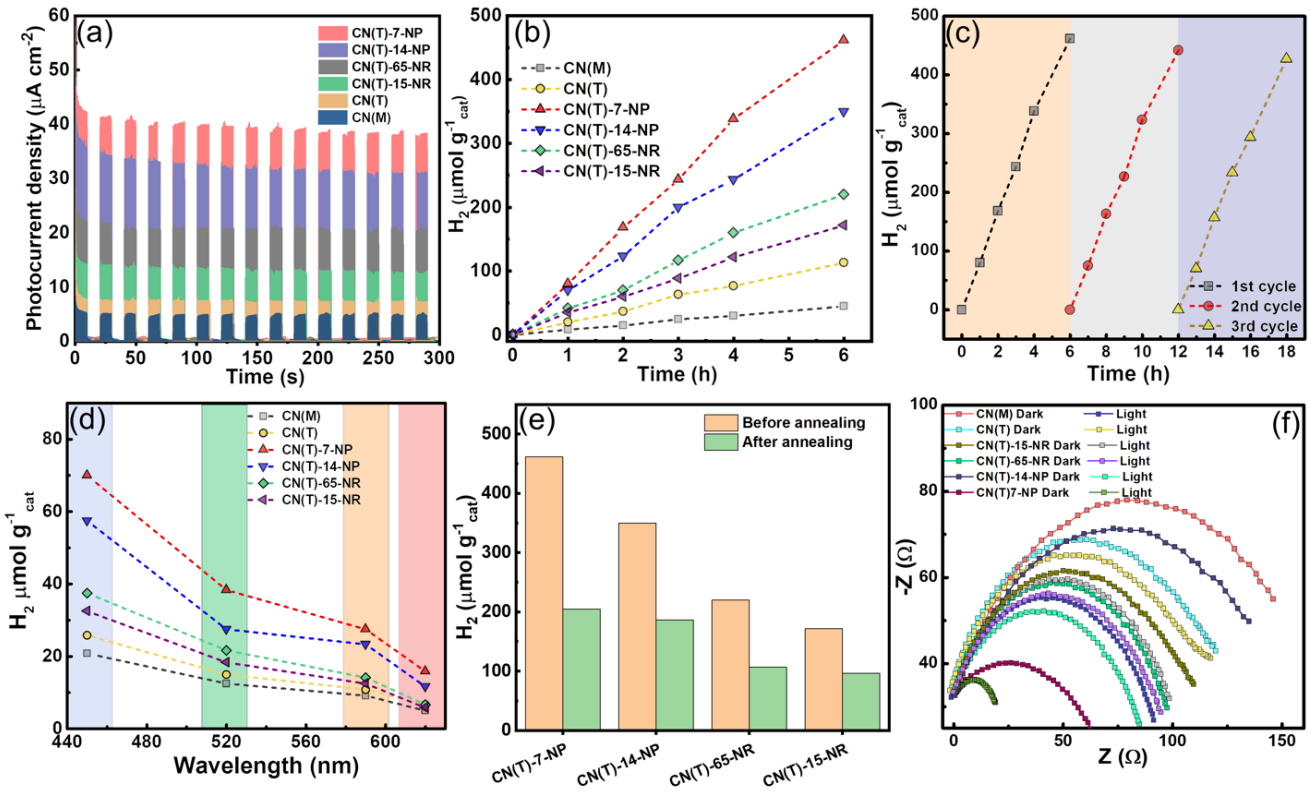

Figure 4. (a) Amperometric photocurrent density vs time (*J-t*) plot of samples showing photo-response during light on-off cycle at +0.6 V applied bias, under solar simulated AM1.5G light irradiation (100 mW cm^{-2}). **(b)** Photocatalytic H_2 evolution profile using CN(M) and CN(T) based catalysts using pure water under AM1.5G irradiation. The experiments were repeated three times and the average values from triplicate data set has been presented. The highest standard deviation values lie within ±10% of H_2 produced in μmol/g_{cat} **(c)** H_2 evolution kinetics after re-purging of the solution using CN(T)-7-NP catalyst. **(d)** Wavelength-dependent H_2 evolution using 450, 520, 590, and 620 (±10) nm LED with a power density of 25 mW cm^{-2} after 6 h. **(e)** H_2 evolution rate after 6 h using fresh and after annealing the samples at 300 °C during 4 h. **(f)** EIS Nyquist plots of samples under dark and AM1.5 G solar simulated light (100 mW cm^{-2}). Inset shows the Randle circuit used to determined fitting paraeters in Table S2.

average lifetime (τ_{avg}) for Au nanostructures containing carbon nitride (Au-CN(T)) was decreased demonstrating facile charge transfer between Au and carbon nitrides.

Diffuse reflectance UV-vis spectra of bare CNs displayed a broad absorption band extending up to 450 nm due to direct band-to-band electronic transition complies with previously reported literature (**Figure 3h**).[26] CN(T) exhibited an increase in total absorption in this band profile compared to CN(M) due to the extended conjugation. The lone pair orbital of uncondensed NH/NH_2 fucntionalities can overlap with C_6N_7 heterocyle to reduce the energy gap between π-π* state leading to better visible light absorption.[45] Interestingly, on gold incorporation into the CN matrix, the absorption band gets slightly redshifted compared to the pristine CN(M) and CN(T). These shifts occur approximately between 460 nm to 475 nm and corroborate well with the change in color of Au-CN(T) nanostructures. Further, the CN(T)-14-NP, CN(T)-65-NR and CN(T)-15-NR materials showed two bands referring to the transversal and longitudinal oscillations characteristic of the Au NP/NRs, centered around 520 and 690 nm. As expected, the CN(T)-7-NP displayed just one characteristic oscillation band of Au at 573 nm due to the spherical 0D structure (**Figure 2g**).[29] The size and shape of Au NPs have a great influence on the photocatalytic activity as the absorption in the visible region is directly related to Au NPs characteristics in the composites. Large NPs scatter light strongly limiting the photocatalytic activity, while for ultrasmall NPs, the plasmon resonance is largely damped and the light absorption cross-section is small.[50] The bandgaps values of the composites, obtained from the Kubelka-Munk function, are close, i.e. CN(T)-65-NR material has the lowest bandgap value of 2.61 eV, followed by CN(T)-14-NP (2.64 eV), CN(T)-7-NP (2.66 eV), CN(T)-15-NR (2.68 eV), CN(T) (2.77 eV) and CN(M) (2.79 eV).[10,51]

We investigated the band-edge positions through Mott-Schottky measurements to understand the intrinsic electronic properties and their capability to donate photoelectrons to reduce water. **Figure 3i** shows the CB positions (flat band potential) which were estimated by extrapolating the linear region of M-S curves under dark conditions, while the VB positions were calculated by adding optical bandgaps to the obtained CB values. The CB position of CN(M) and CN(T) was found to be -0.26 and -0.08 V vs NHE while obtained VB position was 2.53 and 2.69 V vs NHE, respectively. On the other hand, the CB and VB position of Au-CN(T) nanocomposites was also comparable to CN(T) indicating that the electronic properties of these materials are mainly dominated by the bulk carbon nitride matrix. The major difference between Au-CN(T) samples and pure CNs can be observed from the UV-vis spectra, which shows that the LSPR effect of gold in the nanocomposites allows the absorption of a wider fraction of visible region compared to

bare CNs. For facile water photolysis to occur the CB must have a more negative reduction potential than the H^+ (H^+/H_2 - 0.00 V *vs* RHE at pH 7) and VB must have a more positive potential than the water oxidation potential (H_2O/O_2 – 1.23 V vs RHE at pH 7).[10,52] It was observed that the CB and VB positions of the gold composites are well suited for water photolysis to generate H_2.

Photocatalytic Hydrogen Evolution Performance

The photoresponsive behavior of the samples was determined by measuring the photoelectrochemical (PEC) performance of samples using as a photoanode (see ESI for more details). The photocurrent density of samples as a function of time (J-t curve) was measured at 0.6 V vs Ag/AgCl (1.23 V vs RHE; water oxidation potential) during light on-off cycles under AM1.5 G solar irradiation (power density 100 mW cm^{-2}). As can be seen from **Figure 4a**, CN(M) displayed a very poor current density of ~5 µA cm^{-2}. After the introduction of defects states in carbon nitride (CN(T)), the photocurrent response slightly increased (7.5 µA cm^{-2}) suggesting enhanced light absorption in defect-rich CN contributes to effective charge pair generation. This fact was evident from the electrochemical impedance spectroscopy (EIS) measurement which demonstrates smaller charge transfer resistance for the CN(T) sample compared to CN(M). Furthermore, the photocurrent density was significantly boosted after the introduction of Au nanostructures. The highest current density was observed for Au-CN(T) composite with 7 nm Au NPs (CN(T)-7-NP) reaching up to 40 µA cm^{-2}. As the particle size in the composites was increased a detrimental effect in photoelectrochemical response was observed. The PC densities (*J*) for CN(T)-14-NP, CN(T)-65-NR and CN(T)-15-NR were found to be 32, 21 and 13 µA cm^{-2} respectively. The decreased photocurrent values can be explained based on the reduced LSPR features as the sizes increased.[53,54] CN(T)-7-NP, due to its small size, promotes LSPR excitation producing hot electrons, which can be transferred to the CN scaffold. Further, Au NPs due to lower work function than CN also work as electron acceptors and can prolong the charge recombination rate. Compared to inorganic nanostructures, the observed photocurrent values for CN and Au/CN samples were relatively small (microamp range) which was attributed to significant carrier recombination between stacked carbon nitride sheets, therefore all the photogenerated charge cannot reach the electrode and the current values remain small. However, the measurement of photocurrent provides indirect evidence of the relative charge generation rate in the Au-CN composites. The CN(T)-7-NP heterostructure exhibits almost a six-fold increase in the photocurrent compared to the bare CN(T).

The actual performance of the catalysts was tested for the photo-splitting of pure water without any scavengers under AM1.5G irradiation. Expectedly, CN(T)-7-NP displayed the best performance reaching a total H_2 evolution of 461 µmol g^{-1}_{cat} after 6 h (R_{H2}: 76.8 µmol g^{-1} h^{-1}) (**Figure 4b**). The associated

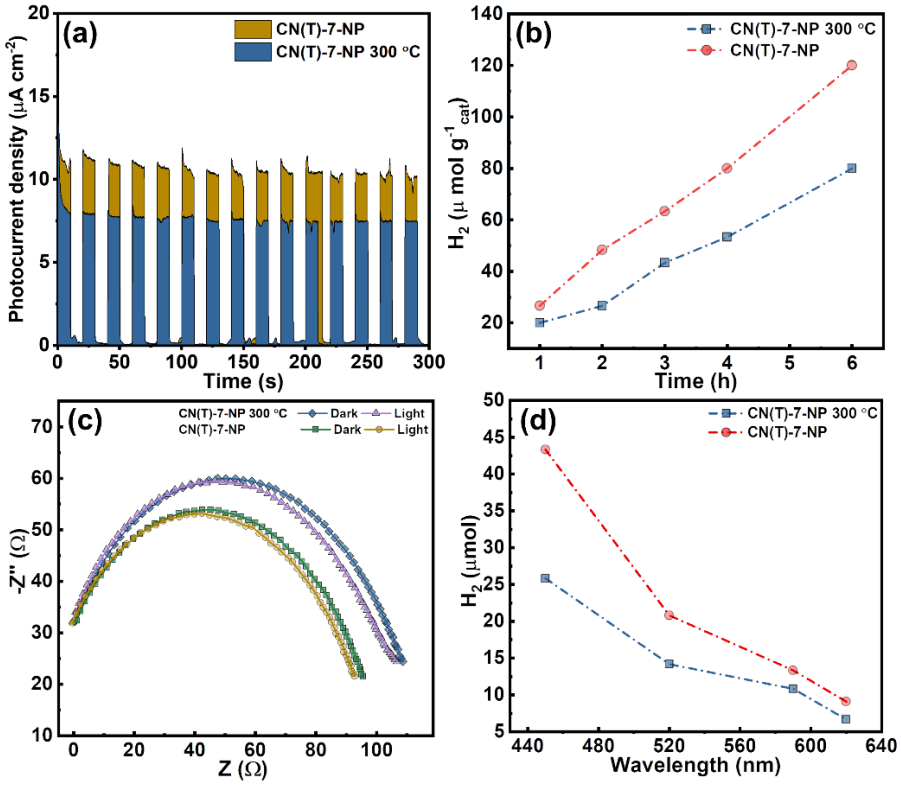

Figure 5. (a) Photocurrent density *vs* time (*J-t*) plot of CN(T)-7-NP and CN(T)-7-NP 300 ºC samples photo response during light on-off cycle at +0.6 V, under AM1.5G light irradiation (100 mW cm^{-2}). **(b)** Photocatalytic hydrogen evolution using CN(T)-7-NP and CN(T)-7-NP 300 ºC catalysts under AM1.5G irradiation. **(c)** EIS Nyquist plots of CN(T)-7-NP and CN(T)-7-NP 300 ºC samples under dark and AM1.5 G solar simulated light (100 mW cm^{-2}). **(d)** Wavelength-dependent H_2 evolution using 450, 520, 590, and 620 (±10) nm LED with a power density of 25 mW cm^{-2} after 6 h.

quantum yield (ϕ_{H2}) was measured to be 0.071. Under identical conditions, the H_2 evolution for CN(M), CN(T), CN(T)-14-NP, CN(T)-65-NR and CN(T)-15-NR was calculated to be 45, 113, 350, 220, and 171 μmol g^{-1}_{cat} after 6 h. It should be noted that the H_2 evolution rate increased linearly demonstrating the stable performance of the catalyst during time. The afforded H_2 evolution rate was significantly high compared to state-of-the-art catalysts used for pure water photo-splitting (**Table S3**). To probe the incessant H_2 performance of the CN(T)-7-NP, recycling experiments were performed by re-purging the evacuated reaction mixture with N_2 followed by irradiation under solar light (**Figure 4c**). The samples displayed a stable H_2 evolution rate for three cycles displaying resilient catalytic performance. The rate of H_2 evolution under different wavelengths was also determined using 450, 520, 590, and 620 nm LEDs with a power density of 25 mW cm^{-2} at the surface of the reaction vessel (**Figure 4d**). Compared to simulated sunlight, the H_2 yield was low for the LED experiments due to low power density and monochromatic radiation. The H_2 evolution rate in monochromatic radiation followed the UV-Vis absorption profile of the samples. All the samples displayed the highest performance at 450 nm. Since carbon nitride absorbs blue light with a band edge at 450 nm, the band-to-band transition remains populated. As the wavelength of incident light was increased the performance tend to decrease due to limited absorption and lesser numbers of electron-hole pairs with lower energy. Though, the rate of H_2 evolution for CN(T)-7-NP remains the highest at all wavelengths, the expected boost at the plasmonic absorption range was absent due to the low loading of nanoparticles embedded in the CN(T) scaffold limiting their absorption.

To deduce the effect of the surface ligand on the photoactivity, the as-synthesized samples were heated at 300 °C to remove the ligand and get bare NPs (**Figure 4e**). The temperature of 300 °C was chosen according to the TG analyses (**Figure 3b**), which is sufficient to remove the ligands from the Au-CN(T) nanocomposites without damaging the CN structures. Surprisingly, the performance of materials after the annealing significantly decreased indicating that the ligands promote better charge transport over the surface of Au. The photoelectrochemical performance, H_2 evolution, EIS and wavelength-dependent H_2 generation rate of CN(T)-7-NP sample are presented in **Figure 5**. Since most of the ligands used in the synthesis are alkyl and carboxyl group-rich ligands such feature provides an insulating environment and concomitantly reduces charge transfer between CN and Au interface. In the case of CN(T)-7-NPs, glutathione was used as a structure-determining agent which can make chemical metal-sulfide bonds, therefore, influencing the Fermi level position. This specific bonding might be facilitating the faster charge migration at the interfaces. This fact was supported by the increased PL decay lifetime of the CN(T)-7-NP_300 °C sample (τ_{avg}- 4.20 ns) compared to CN(T)-7-NP (τ_{avg}-3.98 ns) (**Figure S8b**). Furthermore, the NPs were agglomerated after the removal of ligands during annealing and might be responsible for the reduced activity. The charge separation kinetics and semiconductor-electrolyte interactions were studied by Nyquist plot obtained by EIS under dark and light conditions (**Figure 4f**). The CN(T)-7-NP sample displayed the smallest semicircle arc in the Nyquist plot demonstrating the smallest charge transfer resistance, which represents better semiconductor-to-electrolyte electron transfer kinetics. Various parameters such as series resistance, charge transport resistance, constant phase elements were determined by fitting EIS Randle semicircle as tabluted in **Table S2** in SI. Furthermore, upon irradiation of CN(T)-7-NP sample under AM1.5G light, the arc of the semicircle becomes even smaller suggesting that light irradiation improves the charge transfer kinetics, which concomitantly improves the H_2 generation rate.

From these results, it is evident that N-defects in carbon nitride sites assisted in better photocatalytic performance. This can be correlated to the better visible absorption of light in N

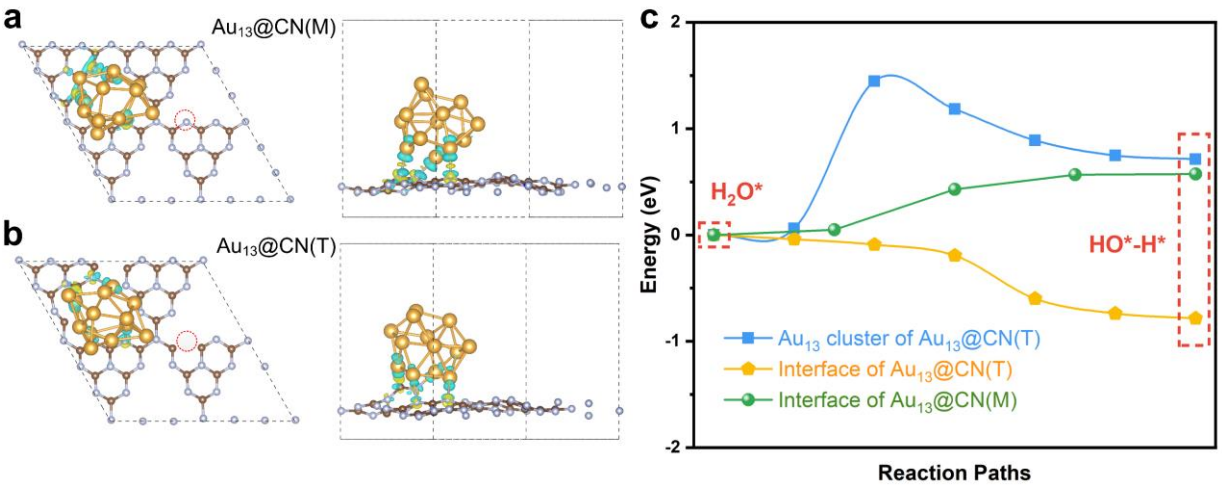

Figure 6. DFT results. **(a-b)** Geometrically optimized atomic structures of Au_{13} cluster supported on CN with (CN(M)) and without defects (CN(T)), including their corresponding charge density difference. Blue and yellow regions represent electron accumulation and loss, respectively. Brown, cyan, and yellow balls indicate C, N, and Au atoms, respectively. The red circle indicates the N-vacancy. **(c)** Reaction mechanism of water splitting on the Au_{13} cluster and the interface between Au_{13} clusters and CN with (CN(M)) and without defects (CN(T)), including their corresponding reaction barriers.

vacancies-rich CN. Despite limited enhancement in visible absorption after the introduction of defects, the catalytic performance of CN(T) was significantly increased, which can be attributed to the stabilization of generated charge carriers in N vacancies as evident from increased carriers lifetime in TRPL.[55] When hybridized with metallic gold, the electron-deficient N vacancies can extract some charge from Au nanoparticles (verified with PL – **Figure S8a**), therefore, providing an active center for the Au attachment and charge transport nanochannels.[56] In contrast to larger nanoparticles and nanorods, the highest H_2 evolution rate was observed for CN(T)-7-NP (76.8 μmol g^{-1} h^{-1}), which can be explained based on increased visible absorption due to LSPR.[57,58] As we know in large metal nanoparticles, the inter-band energy separation remains too low and therefore electrons can absorb the large wavelength of light and reach an excited state. However, due to extended d-sp orbital conjugation and lack of enough energy, these charge carriers remain confined to bulk metal and can not surmount the metal-semiconductor Schottky barrier. Therefore, visible light absorption in large nanoparticles remains unproductive and these particles increase photoactivity merely due to their excellent electron-capturing activity. When the particle size is reduced below 20 nm, the quantum confinement effect becomes dominant and d-sp separation becomes large.[59] In such cases, only transitions energetic enough to overcome this energy barrier can take place and generated electrons have higher energy (hot electrons) to overcome the Schottky barrier. Furthermore, large available surfaces in smaller NPs and better interaction with carbon nitride surface further boost the photocatalytic performance.

Computational studies

To get more insights into the outstanding catalytic performance of Au nanostructures supported on defect-enriched carbon nitride (CN(T)) for water splitting, density functional theory (DFT) calculations were performed. We built the Au_{13} cluster as an Au nanostructure supported into CN with and without a nitrogen-vacancy defect, as shown in **Figure 6a-b**. The binding energy between the Au nanostructure and the CN substrates could be used as an indicator for the stability of the catalyst system. For Au_{13}@CN without defects, the binding energy value is -4.23 eV, while it is -6.09 eV for Au_{13}@CN with defects. This signifies that the defects could make the designed catalyst more stable, which is crucial during the catalytic process. Moreover, the stronger interaction between Au_{13} and defects-rich CN results in more electrons (0.19 *e*) transferred from Au_{13} to CN with defects, compared to that (0.04 *e*) between Au_{13} and CN without defects, which facilitates the separation of the e^-/h^+ pair after light excitation. As shown in **Figure S9**, compared with Au_{13}@CN without defects, more significant hybridizations between CN-p orbits and Au-d orbits are presented around the Fermi level for the system of Au_{13}@CN with defects, demonstrated the stronger interaction between CN with defects and Au_{13} cluster. Furthermore, the d band center value of the Au_{13} cluster achieved from **Figure S10** are -2.88 eV and -2.65 eV for Au_{13}@CN with and without defects, respectively. It means that the Au_{13} cluster in Au_{13}@CN with defects has a higher catalytic activity because its d band center is closer to the Fermi level, which is consistent with our experimental results.

The reaction mechanism of water splitting was considered at the interface between Au_{13} clusters and CN with and without defects, as shown in **Figure 6c**. On the Au_{13}@CN without defects, water splitting is found to be an endothermic reaction with a barrier of 0.57 eV, while it is a spontaneous reaction at the interface between Au_{13} clusters and CN in Au_{13}@CN with defects. This implies that the defects in CN(T) promote water splitting, which is consistent with the experimental results. More importantly, we also considered the active sites far away from the interfaces for water splitting. The corresponding reaction barrier is 1.45 eV, which is too high for the catalytic reaction to occur. Therefore, from the computation studies, we find that the interface is the key active site for water splitting in these nano heterostructures. The smaller Au NPs have more interfaces that are accessible compared to the larger Au nanostructures. Thus, it can be concluded that due to larger exposed interfacial sites and higher LSPR effect, the CN(T)-7-NP excels in photocatalytic performance among the composites, matching the state-of-art H_2 generation rates among related catalytic systems. Despite having a slightly larger charge carrier recombination rate (as evident from PL), the defective CN(T) provides better interaction with the Au surface for hot electron transfer and provides more active interfacial sites that lower the energy barrier for the water splitting pathway. DFT calculations demonstrate facile charge transfer takes place between the small Au NPs to CN(T) interface due to N vacancies, which also lower the energy barrier for H_2 generation resulting in increased photocatalytic performance.

Conclusions

In summary, we have demonstrated the effects of the size and shape of Au metal in the photocatalytic HER under visible light through the syntheses of four Au/CNs heterostructures. More importantly, we scrutinized the positive influence of the surface ligands in the complex balance between LPSR and interfacial charge separation. The CN(T)-7-NP, synthesized by incipient wetness method, with Au NPs of an average size of 7 nm supported on defect-enriched carbon nitride (CN(T)), delivered optimum H_2 production performance of 76.8 μmol g^{-1} h^{-1} from pure water under visible light (> 420 nm) irradiation, without using any scarifical agents. CN(T)-7-NP material possess the highest absorption in the visible region, which can be related to prominent size dependent LSPR. Furthermore, reduced photocatalytic HER performance of Au NPs and Au NRs on CN(T) after ligand removal at 300 °C, corroborate that the ligands promote better charge transport on Au surface. In addition, DFT calculations suggest better interactions and facile charge transfer between defect enriched CN(T) and Au heterointerface and establishment of a low energy barrier pathway for water splitting. The improved visible absorption and e^-/h^+ pairs separation reinforced by ligands in Au/CNTs allow the harvesting of visible light to generate H_2 at an elevated rate. The

work presented here will guide future catalyst designs for green hydrogen production from pure water.

Author contributions

I.F.S.: conceptualization, methodology, investigation, experiments and analyses, writing—original draft, writing—review & editing. S.R.: conceptualization, methodology, investigation, experiments and analyses, visualization & computational studies, writing—original draft, writing—review & editing. P. K.: conceptualization, methodology, investigation, experiments and analyses, writing—original draft, writing—review & editing. Z. C.: visualization & computational studies, writing—review & editing. I.F.T.: conceptualization, methodology, investigation, experiments and analyses, supervision, writing—review & editing. A.M.C.M.: writing—review & editing. L.M.A.: experiments and analyses, writing—review & editing. L.O.L.: supervision, writing—review & editing. H.O.S.: conceptualization, supervision, writing—review & editing. C.V.S.: visualization & computational studies, writing—review & editing. A.P.C.T.: conceptualization, methodology, investigation, supervision, writing—review & editing. M.G.K.: supervision, writing—review & editing. P.M.A.: supervision, writing—review & editing.

# Ingrid F. Silva, Soumyabrata Roy, Pawan Kumar contributed equally to this work.

Conflicts of Interest

There are no conflicts to declare.

Acknowledgments

IFS, IFT, LMA, LOL, HOS and APCT are grateful to the Brazilian funding agencies Conselho Nacional de Desenvolvimento Cientifico e Tecnológico (CNPq) (Processes 423196/2018-9 and 403064/2021-0), the Fundação de Amparo à Pesquisa do Estado de Minas Gerais (FAPEMIG), the Coordenação de Aperfeiçoamento de Pessoal de Nível Superior (CAPES) and the Fundação de Amparo à Pesquisa do Estado de São Paulo (FAPESP) (Processes 2020/14741-6 and 2021/11162-8) for financial support. The authors would like to thank the Microscopy Center at UFMG for the microscopy images. PK and MGK would like to acknowledge the financial support from Canada First Research Excellence Fund (CFREF) at the University of Calgary. Part of the research described in this paper was performed at the Canadian Light Source (project: 35G12344), a national research facility of the University of Saskatchewan, which is supported by the Canada Foundation for Innovation (CFI), the Natural Sciences and Engineering Research Council (NSERC), the National Research Council (NRC), the Canadian Institutes of Health Research (CIHR), the Government of Saskatchewan, and the University of Saskatchewan.

References

1 M. Schröder, K. Kailasam, J. Borgmeyer, M. Neumann, A. Thomas, R. Schomäcker and M. Schwarze, *Energy Technol.*, 2015, **3**, 1014–1017.
2 G. Gao, Y. Jiao, F. Ma, Y. Jiao, E. Waclawik and A. Du, *J. Catal.*, 2015, **332**, 149–155.
3 F. Nichols, Q. Liu, J. Sandhu, Z. Azhar, R. Cazares, R. Mercado, F. Bridges and S. Chen, *J. Mater. Chem. A*, 2022, **10**, 5962–5970.
4 I. F. Teixeira, N. V. Tarakina, I. F. Silva, N. López-Salas, A. Savateev and M. Antonietti, *Adv. Sustain. Syst.*, 2022, **2100429**, 1–8.
5 R. W. Howarth and M. Z. Jacobson, *Energy Sci. Eng.*, 2021, **9**, 1676–1687.
6 IEA – International Energy Agency, https://www.iea.org/reports/renewables-2020.
7 L. Niu, J. Du, D. Jiang, H. Du, X. Lin, J. Xu, Z. Li, C. Zhu, L. Gu, H. Bi and Y. Yuan, *Catal. Letters*, 2022, **152**, 669–678.
8 G. Liao, Y. Gong, L. Zhang, H. Gao, G.-J. Yang and B. Fang, *Energy Environ. Sci.*, 2019, **12**, 2080–2147.
9 P. Jiménez-Calvo, V. Caps, M. N. Ghazzal, C. Colbeau-Justin and V. Keller, *Nano Energy*, 2020, **75**, 104888.
10 I. F. Teixeira, E. C. M. Barbosa, S. C. E. Tsang and P. H. C. Camargo, *Chem. Soc. Rev.*, 2018, **47**, 7783–7817.
11 P. Jiménez-Calvo, C. Marchal, T. Cottineau, V. Caps and V. Keller, *J. Mater. Chem. A*, 2019, **7**, 14849–14863.
12 I. F. Teixeira, N. V. Tarakina, I. F. Silva, G. A. Atta Diab, N. L. Salas, A. Savateev and M. Antonietti, *J. Mater. Chem. A*, 2022, **10**, 18156–18161.
13 Y. Xie, Y. Li, Z. Huang, J. Zhang, X. Jia, X. S. Wang and J. Ye, *Appl. Catal. B Environ.*, 2020, **265**, 118581.
14 Y. Zhang, H. Gong, G. Li, H. Zeng, L. Zhong, K. Liu, H. Cao and H. Yan, *Int. J. Hydrogen Energy*, 2017, **42**, 143–151.
15 C. Wan, L. Zhou, S. Xu, B. Jin, X. Ge, X. Qian, L. Xu, F. Chen, X. Zhan, Y. Yang and D. guo Cheng, *Chem. Eng. J.*, 2022, **429**, 132388.
16 J. Wang, Y. Chen, Y. Shen, S. Liu and Y. Zhang, *Chem. Commun.*, 2017, **53**, 2978–2981.
17 F. Zeng, W. Q. Huang, J. H. Xiao, Y. Y. Li, W. Peng, W. Hu, K. Li and G. F. Huang, *J. Phys. D. Appl. Phys.*, 2019, **52**, 025501.
18 J. Chen, C. L. Dong, Y. Du, D. Zhao and S. Shen, *Adv. Mater. Interfaces*, 2015, **2**, 1500280.
19 W. Hou and S. B. Cronin, *Adv. Funct. Mater.*, 2013, **23**, 1612–1619.
20 Z. Guo, F. Dai, H. Yin, M. Zhang, J. Xing and L. Wang, *Colloids Interface Sci. Commun.*, 2022, **48**, 100615.
21 R. B. Grubbs, *Polym. Rev.*, 2007, **47**, 197–215.
22 R. D. Neal, R. A. Hughes, P. Sapkota, S. Ptasinska and S. Neretina, *ACS Catal.*, 2020, **10**, 10040–10050.
23 C. W. Moon, M. J. Choi, J. K. Hyun and H. W. Jang, *Nanoscale Adv.*, 2021, **3**, 5981–6006.
24 L. Lu, H. Zheng, Y. Li, Y. Zhou and B. Fang, *Chem. Eng. J.*, 2023, **451**, 138668.
25 H. Tian, X. Liu, Z. Liang, P. Qiu, X. Qian, H. Cui and J. Tian, *J. Colloid Interface Sci.*, 2019, **557**, 700–708.
26 I. F. Silva, I. F. Teixeira, R. D. F. Rios, G. M. do Nascimento, I. Binatti, H. F. V. Victória, K. Krambrock, L. A. Cury, A. P. C. Teixeira and H. O. Stumpf, *J. Hazard. Mater.*, 2021, **401**, 123713.
27 C. A. Simpson, K. J. Salleng, D. E. Cliffel and D. L. Feldheim, *Nanomedicine Nanotechnology, Biol. Med.*, 2013, **9**, 257–263.
28 J. Turkevich, P. C. Stevenson and J. Hillier, *Discuss. Faraday Soc.*, 1951, **11**, 55–75.
29 B. Nikoobakht and M. A. El-Sayed, *Chem. Mater.*, 2003, **15**, 1957–1962.

30 Q. Liang, M. Zhang, C. Liu, S. Xu and Z. Li, *Appl. Catal. A Gen.*, 2016, **519**, 107–115.
31 S. Cao, B. Fan, Y. Feng, H. Chen, F. Jiang and X. Wang, *Chem. Eng. J.*, 2018, **353**, 147–156.
32 C. Y. Wang, K. Maeda, L. L. Chang, K. L. Tung and C. Hu, *Carbon N. Y.*, 2022, **188**, 482–491.
33 X. Qin, W. Lu, G. Chang, Y. Luo, A. M. Asiri, A. O. Al-Youbi and X. Sun, *Gold Bull.*, 2012, **45**, 61–67.
34 Y. Kang, Y. Yang, L. C. Yin, X. Kang, L. Wang, G. Liu and H. M. Cheng, *Adv. Mater.*, 2016, **28**, 6471–6477.
35 K. K. R. Datta, B. V. S. Reddy, K. Ariga and A. Vinu, *Angew. Chemie*, 2010, **122**, 6097–6101.
36 Y. Chang, Z. Liu, X. Shen, B. Zhu, D. K. Macharia, Z. Chen and L. Zhang, *J. Hazard. Mater.*, 2018, **344**, 1188–1197.
37 C. F. Holder and R. E. Schaak, *ACS Nano*, 2019, **13**, 7359–7365.
38 I. F. Silva, R. D. F. Rios, O. Savateev and I. F. Teixeira, *ACS Appl. Nano Mater.*, 2023, **6**, 9718–9727.
39 P. Veerakumar, N. Dhenadhayalan, K. C. Lin and S. Bin Liu, *ChemistrySelect*, 2017, **2**, 1398–1408.
40 Z. Chen, A. Savateev, S. Pronkin, V. C. W. Papaefthimiou, M. G. Willinger, E. Willinger, D. Neher, M. Antonietti and D. Dontsova, *Adv. Mater.*, 2017, **29**, 1700555.
41 K. Wang, Q. Li, B. Liu, B. Cheng, W. Ho and J. Yu, *Appl. Catal. B Environ.*, 2015, **176**–**177**, 44–52.
42 P. Yang, H. Ou, Y. Fang and X. Wang, *Angew. Chem. Int. Ed.*, 2017, **56**, 3992–3996.
43 Y. Hong, L. Wang, E. Liu, J. Chen, Z. Wang, S. Zhang, X. Lin, X. Duan and J. Shi, *Inorg. Chem. Front.*, 2020, **7**, 347–355.
44 Y. Zhang, Q. Pan, G. Chai, M. Liang, G. Dong, Q. Zhang and J. Qiu, *Sci. Rep.*, 2013, **3**, 1–8.
45 P. Kumar, E. Vahidzadeh, U. K. Thakur, P. Kar, K. M. Alam, A. Goswami, N. Mahdi, K. Cui, G. M. Bernard, V. K. Michaelis and K. Shankar, *J. Am. Chem. Soc.*, 2019, **141**, 5415–5436.
46 L. C. Chen, C. Y. Teng, C. Y. Lin, H. Y. Chang, S. J. Chen and H. Teng, *Adv. Energy Mater.*, 2016, **6**, 1600719.
47 B. Choudhury, K. K. Paul, D. Sanyal, A. Hazarika and P. K. Giri, *J. Phys. Chem. C*, 2018, **122**, 9209–9219.
48 J. Bian, J. Li, S. Kalytchuk, Y. Wang, Q. Li, T. C. Lau, T. A. Niehaus, A. L. Rogach and R. Q. Zhang, *ChemPhysChem*, 2015, **16**, 954–959.
49 J. Xu, M. Shalom, F. Piersimoni, M. Antonietti, D. Neher and T. J. K. Brenner, *Adv. Opt. Mater.*, 2015, **3**, 913–917.
50 Y. Guo, H. Jia, J. Yang, H. Yin and Z. Yang, *Phys. Chem. Chem. Phys.*, 2018, **20**, 22296–22307.
51 S. Cao, J. Low, J. Yu and M. Jaroniec, *Adv. Mater.*, 2015, **27**, 2150–2176.
52 J. Fu, J. Yu, C. Jiang and B. Cheng, *Adv. Energy Mater.*, 2018, **8**, 1–31.
53 H. Lee, K. Song, M. Lee and J. Y. Park, *Adv. Sci.*, 2020, **7**, 1–8.
54 V. Juve, M. F. Cardinal, A. Lombardi, A. Crut, P. Maioli, L. M. Liz-Marzan, N. Del Fatti and F. Vallee, *Nano Lett.*, 2013, **13**, 2234–2240.
55 P. Niu, G. Liu and H. M. Cheng, *J. Phys. Chem. C*, 2012, **116**, 11013–11018.
56 S. Wu, Z. Chen, K. Liu, W. Yue, L. Wang and J. Zhang, *ChemSusChem*, 2020, **13**, 3455–3461.
57 V. Amendola, R. Pilot, M. Frasconi, O. M. Maragò and M. A. Iatì, *J. Phys. Condens. Matter*, 2017, **29**, 203002.
58 A. P. Manuel, A. Kirkey, N. Mahdi and K. Shankar, *J. Mater. Chem. C*, 2019, **7**, 1821–1853.
59 S. Lv, Y. Du, F. Wu, Y. Cai and T. Zhou, *Nanoscale Adv.*, 2022, **4**, 2608–2631.